

THE DRIVING SCALE – DENSITY DECORRELATION SCALE RELATION IN A TURBULENT MEDIUM

SHMUEL BIALY

Harvard-Smithsonian Center for Astrophysics, 60 Garden St., Cambridge, MA, 02138

BLAKESLEY BURKHART

Department of Physics and Astronomy, Rutgers, The State University of New Jersey, 136 Frelinghuysen Rd, Piscataway, NJ 08854 and
 Center for Computational Astrophysics, Flatiron Institute, 162 Fifth Avenue, New York, NY 10010

Accepted for publication in ApJ. Letters

ABSTRACT

Density fluctuations produced by supersonic turbulence are of great importance to astrophysical chemical models. A property of these density fluctuations is that the two point correlation function decreases with increasing scale separation. The relation between the density decorrelation length scale (L_{dec}) and the turbulence driving scale (L_{drive}) determines how turbulence affects the density and chemical structures in the interstellar medium (ISM), and is a key component for using observations of atomic and molecular tracers to constrain turbulence properties. We run a set of numerical simulations of supersonic magnetohydrodynamic turbulence, with different sonic Mach numbers ($\mathcal{M}_s = 4.5, 7$), and driven on varying scales ($1/2.5, 1/5, 1/7$) the box length. We derive the $L_{\text{dec}} - L_{\text{drive}}$ relation as a function of Mach number, driving scale, and the orientation of the line-of-sight (LOS) in respect to the magnetic-field. We find that the mean ratio $L_{\text{dec}}/L_{\text{drive}} = 0.19 \pm 0.10$, when averaged over snapshots, Mach numbers, driving lengths, and the three LOSs. For LOS parallel to the magnetic field the density structures are statistically smaller and the $L_{\text{dec}} - L_{\text{drive}}$ relation is tighter, with $L_{\text{dec}}/L_{\text{drive}} = 0.112 \pm 0.024$. We discuss our results in the context of using observations of chemical tracers to constrain the dominant turbulence driving scale in the ISM.

1. INTRODUCTION

Understanding turbulence in galaxies is of central importance to a number of areas of astrophysical interest including star formation (e.g., Krumholz et al. 2009; Ostriker et al. 2010; Burkhardt et al. 2015c), cosmic ray acceleration and diffusion Schlickeiser (2002); Lazarian & Yan (2014); Xu et al. (2016), and accretion disks around planets, stars and black holes Balbus & Hawley (1991); Hughes et al. (2010); Ross et al. (2017). Compressible turbulence is ubiquitous throughout the interstellar medium (ISM) of galaxies from scales of at least tens of parsecs down to the sub-parsec scales (Armstrong et al. 1995; McKee & Ostriker 2007; Lazarian 2007; Chepurnov et al. 2010; Krumholz 2014; Burkhardt et al. 2015a). Turbulence in the ISM may be driven by multiple energy injection sources on different scales (Elmegreen & Scalo 2004; Chepurnov et al. 2015; Pingel et al. 2018), from disk instabilities and supernova acting on the largest scales (Krumholz & Burkhardt 2016) to stellar winds and jets on sub-cloud scales (Offner et al. 2014). Considering the wide range of scales galactic turbulence affects there has been significant effort to connect observed levels of turbulence with theoretical predictions and simulations (Goldreich & Sridhar 1995; Cho & Lazarian 2003; Federrath et al. 2008; Burkhardt et al. 2010; Correia et al. 2016; Herron et al. 2017). However, it is still unclear which driving mechanism dominates the turbulent energy budget in the ISM (Krumholz 2014) and on what scales the turbulence is dissipated (Burkhardt et al. 2015b).

An important feature of a compressible turbulent cascade is that density fluctuations exhibit statistical correlations in relation to the driving scale (Burkhardt et al. 2009; Portillo et al. 2018). Numerical and analytic studies found that the correlation of density fluctuations decreases with increasing spatial separation (Kowal et al. 2007, Bialy et al. 2017, hereafter BBS). The characteristic scale over which the correlation de-

creases is the density decorrelation scale, L_{dec} , and it is found to be of order of the driving scale, L_{drive} ,

$$\frac{L_{\text{dec}}}{L_{\text{drive}}} = \phi \quad (1)$$

with $\phi \approx 0.1 - 0.3$ (Vazquez-Semadeni & Garcia 2001, hereafter VG, Fischera & Dopita 2004, Kowal et al. 2007, BBS). The exact value of ϕ depends on the method used to measure the decorrelation scale, for example, VG define L_{dec} as the point at which the autocorrelation function (ACF) falls to a fraction 0.1 of its initial value, whereas BBS derive L_{dec} using an analytic model that describes the correlation of the smoothed-density field as a function of the smoothing-length (see §2 below; cf. Squire & Hopkins 2017).

Importantly, as discussed by BBS and Bialy et al. (2019), L_{dec} may be constrained from observations of the column density probability density function (PDF) of various atomic and molecular tracers (H, H₂, OH⁺, OH⁺, H₂⁺, Ar⁺). This is because the chemical reactions in the ISM are sensitive to the gas density and its structure. In particular, the absorption of ultraviolet (UV) radiation by H₂ lines (i.e., H₂ self-shielding) is very sensitive to the length-scales of density fluctuations. In turn, other molecular species depend on the H₂ abundance, and are therefore also sensitive to L_{dec} . Given a robust relation between L_{dec} and L_{drive} , observations of chemical tracers may be used to constrain the turbulence driving scale (see Fig. 4 and §5.1 below).

However, previous numerical studies have obtained L_{dec} considering only large driving scales, of order of the simulation box-size. In this Letter, we use a large set of supersonic MHD simulations, driven on various scales: (1) large-scale $k_{\text{drive}} = 2.5$ driving (we denote the wavenumber $k \equiv 1/L_{\text{box}}$), (2) intermediate scale $k_{\text{drive}} = 5$ driving, and (3) small scale $k_{\text{drive}} = 7$ driving, and derive the $L_{\text{dec}} - L_{\text{drive}}$ relation as a

function of k_{drive} . For each driving-scale we further investigate the dependence of the density structures on the line-of-sight (LOS) orientation, parallel and perpendicular to the large scale magnetic field, and on the sonic Mach number.

This Letter is organized as follows: in §2 we provide a theoretical overview for methods for deriving the decorrelation scale. In §3 we describe our numerical set up. In §4 we present results for the density structures and the decorrelation scale, and their dependence on LOS orientation and driving scale. We discuss our results in §5, and conclude in §6.

2. THEORETICAL BACKGROUND

The decorrelation scale, L_{dec} , is the characteristic scale over which density correlations decrease. We consider two definitions for L_{dec} , (1) via the smoothed-density method (BBS), and (2) using the ACF (i.e., VG). The smoothed-density method was developed for modeling the distribution of integrated column densities of chemical species and inferring properties of the 3D density field (BBS). The idea is quite intuitive: if we smooth (average) the density over a scale ℓ , and let ℓ vary from small to large, we expect the dispersion of the smoothed density to decrease with increasing ℓ , as more density fluctuations are smoothed-out within the smoothing length

More quantitatively, given the field $x \equiv n/\langle n \rangle$ (i.e., normalized density), we define the smoothed-density

$$x_\ell(\ell) \equiv \frac{\int_z^{z+\ell} x \, dz'}{\ell}, \quad (2)$$

where ℓ is the smoothing length and z the line-of-sight (LOS) direction along which the density is smoothed. If x is a 3D field, then x_ℓ is also a 3D field but unlike x , x_ℓ also depends on ℓ . The distribution of x_ℓ is tightly related to that of the column density of slab of size ℓ : $N = x_\ell \langle n \rangle \ell$.

Let σ_x and $\sigma_{x_\ell}(\ell)$ be the standard deviations (SDs) of x and x_ℓ . To obtain an analytic description for $\sigma_{x_\ell}(\ell)$, we assume that the correlation may be described with a single parameter, L_{dec} , such that when $\ell < L_{\text{dec}}$ the density is correlated, while when $\ell \geq L_{\text{dec}}$ the density is uncorrelated¹. The number of independent density cells along a LOS of length ℓ is

$$\mathcal{N}(\ell) \approx \ell/L_{\text{dec}} + 1, \quad (3)$$

and the x_ℓ distribution may be viewed as the sampling distribution of the mean (encountered in the error estimation of repeated measurements; Barlow 1989). The x_ℓ SD obeys

$$\frac{\sigma_{x_\ell}}{\sigma_x} = \frac{1}{\sqrt{\mathcal{N}(\ell)}} = \frac{1}{\sqrt{1 + \ell/L_{\text{dec}}}}. \quad (4)$$

In the limit $\ell/L_{\text{dec}} \ll 1$, the smoothing length is smaller than a single density fluctuation, $\mathcal{N} \approx 1$, and $\sigma_{x_\ell} \rightarrow \sigma_x$. In the other extreme, when $\ell/L_{\text{dec}} \gg 1$, $\mathcal{N} \gg 1$, many turbulent fluctuations are smoothed-over within ℓ , and σ_{x_ℓ}/σ_x vanishes. For more details and examples, see §4 in BBS. See also Squire & Hopkins (2017) for an alternative derivation of the density PDF as a function of scale.

Another way to define L_{dec} is from the ACF of the density field. The ACF generally decreases with increasing lag, and

¹ This is obviously an approximation, as in a realistic density field that arises from turbulent cascade, the correlation does not fall abruptly, and it may vary with time and space. Nevertheless, as shown by BBS, this model provides a good approximation for the complicated density field found in the simulations.

we may define L_{dec} as the point at which the ACF falls below some fraction ε of its (initial) maximum value. This method depends on the somewhat arbitrary choice of ε . Interestingly, as we show below, the suggestion of VG to use $\varepsilon = 0.1$ yields L_{dec} values that are in very good agreement with those obtained via our smoothed-density method (§4.3).

3. NUMERICAL METHOD

3.1. MHD simulations

We run 3D numerical simulations of isothermal compressible MHD turbulence. The code and setup is similar to that of a number of past works (Kowal et al. 2007, Burkhart et al. 2009, BBS). We refer to these works for the details of the numerical set-up and here provide a short overview. The code is a third-order accurate ENO scheme which solves the ideal MHD equations in a periodic box with purely solenoidal driving (?). The magnetic field consists of the uniform background field and a turbulent field, i.e: $\mathbf{B} = \mathbf{B}_0 + \mathbf{b}$ with the magnetic field initialized along a single preferred direction. We run two sets of simulations, with a sonic Mach number $\mathcal{M}_s = 4.5$ and $\mathcal{M}_s = 7$. While previous studies used driving on large scales, with $k_{\text{drive}} = 2 - 2.5$, here, for each Mach number, we run several simulations, each of which driven on a different driving scale, of $k_{\text{drive}} = 2.5, 5$, and 7 . We also ran simulations of $k_{\text{drive}} = 10$ but for this high k_{drive} the results do not robustly converge and thus we do not discuss this simulation further. The Alfvénic Mach number in all the simulations is $\mathcal{M}_A = 0.7$. To test numerical convergence we also run simulations with various resolutions. For the $\mathcal{M}_s = 4.5$ simulations we run, $N_{\text{res}} = 256^3, 512^3$ and 1024^3 resolution elements. For the $\mathcal{M}_s = 7$ simulation we only run 1024^3 resolution.

3.2. Calculating L_{dec} for the MHD boxes

For each simulation, characterized by $(\mathcal{M}_s, k_{\text{drive}}, N_{\text{res}})$ we calculate L_{dec} as follows:

- (1) calculate σ_x for that simulation.
- (2) calculate $\sigma_{x_\ell}(\ell)$: We choose ℓ , and integration orientation (hereafter denoted by line-of-sight, LOS). We pick 5×10^5 random locations (cells) in the simulation and for each location we compute the smoothed density x_ℓ using Eq. (2) (we use periodic boundaries). This gives the x_ℓ distribution at scale ℓ . We repeat this for ℓ values ranging from 0 to 1 (we adopt units normalized to the box length) and calculate σ_{x_ℓ} as a function of ℓ .
- (3) Fit Eq. (4) to the numerical data, $\sigma_{x_\ell}(\ell)/\sigma_x$ as a function of ℓ , with L_{dec} being the best-fitting parameter that minimizes χ^2 .

We follow the procedure above for three LOS orientations, 1 parallel and 2 perpendicular to \mathbf{B}_0 . For each simulation and LOS orientation, we repeat the steps above 5 times for 5 time snapshots and adopt the average L_{dec} as the value of the decorrelation scale. For the error we sum in quadrature the error from the χ^2 fitting (step 3), and the SD L_{dec} over the 5 time snapshots. In conclusion we obtain $L_{\text{dec}} \pm \Delta L_{\text{dec}}$ for different $\mathcal{M}_s, k_{\text{drive}}, N_{\text{res}}$, and LOS orientation.

4. RESULTS

In this section we present results for the density structures in the turbulent boxes, and particularly the dependence of the density decorrelation scale, L_{dec} , on driving scale, LOS orientation, and resolution.

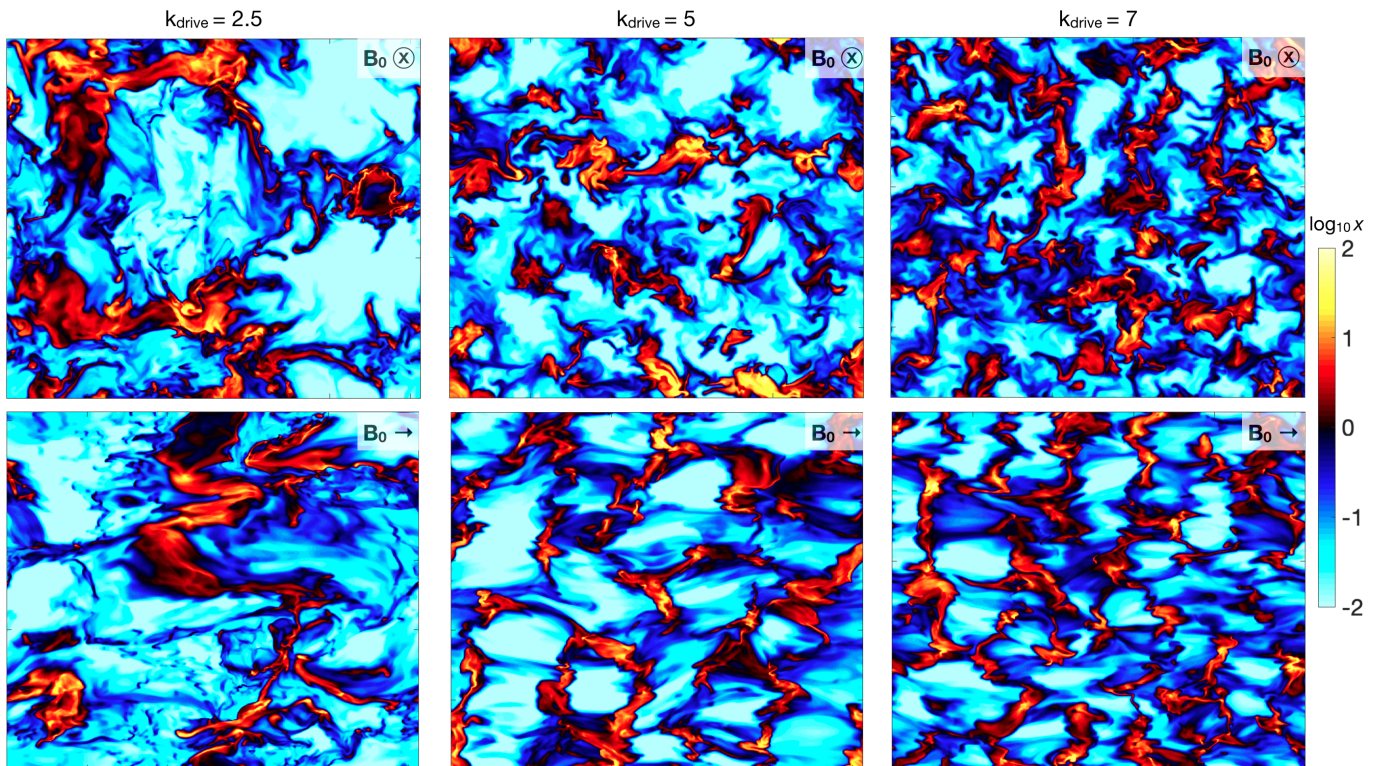


FIG. 1.— Density cuts through the $\mathcal{M}_s = 4.5$, $k_{\text{drive}} = 2.5$ (left), $k_{\text{drive}} = 5$ (middle) and $k_{\text{drive}} = 7$ (right) simulations. In the top panels \mathbf{B}_0 is directed into the plane and in the bottom from left to right. The colorscale corresponds to $\log_{10} x \equiv \log_{10} n/\langle n \rangle$.

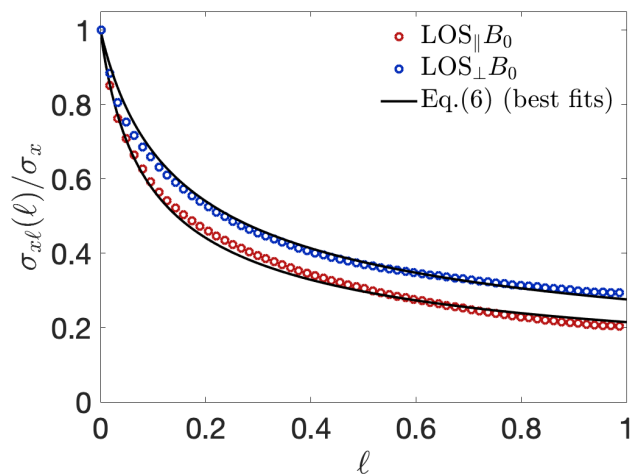


FIG. 2.— The smoothed-density SD normalized to the density SD, as a function of smoothing length, ℓ (in units of box-length), for the $\mathcal{M}_s = 4.5$, $k_{\text{drive}} = 2.5$, $N_{\text{res}} = 1024^3$ simulation. The red and blue points correspond to $\text{LOS}_{\parallel} \mathbf{B}_0$ and $\perp \mathbf{B}_0$, and the black curves are fits to Eq. (4), yielding $L_{\text{dec}} = (4.85, 8.25) \times 10^{-2}$, respectively.

4.1. Density Slices

We start with some visual examples of the data. In Fig. 1 we show density slices for the $\mathcal{M}_s = 4.5$, $N_{\text{res}} = 1024^3$, $k_{\text{drive}} = 2.5$ (left), 5 (middle), and 7 (right) simulations. Comparing the panels left-to-right, it is evident that density structures are typically smaller as the driving scale decreases. This is expected as the density fluctuations develop as a result of the driving process. In the upper panels, we see that density structures are relatively isotropic (compared to the lower panels).

This is because in these panels \mathbf{B}_0 is directed into the plane and thus there is no preferred direction. Thus the structure is more reminiscent of pure hydro turbulence. On the other hand in the lower panel, where \mathbf{B}_0 is in the plane, the density structures are not isotropic and tend to have their shorter dimension along \mathbf{B}_0 . This behavior makes sense physically as the gas may stream more freely in directions along the magnetic field and thus gas compressions are more efficient. As we show in §4.3, our calculated decorrelation scale as a function of k_{drive} and LOS orientation captures these trends in a quantitative manner.

4.2. The standard deviation of the smoothed and non-smoothed density

In Fig. 2 we show an example of the calculated $\sigma_{x\ell}/\sigma_x$ as a function of the smoothing length ℓ , for the $\mathcal{M}_s = 4.5$, $k_{\text{drive}} = 2.5$, $N_{\text{res}} = 1024^3$ simulation. The red points correspond to the $\text{LOS}_{\parallel} \mathbf{B}_0$ and the blue points to a $\text{LOS}_{\perp} \mathbf{B}_0$. The black curves are the best χ^2 fits to Eq. (4) which yield L_{dec} for these LOS orientations. As expected, $\sigma_{x\ell}/\sigma_x$ approaches unity in limit $\ell \rightarrow 0$ as smoothing becomes ineffective. As ℓ increases, more of the density structures are averaged-out and $\sigma_{x\ell}$ decreases. $\sigma_{x\ell}$ falls faster for the $\text{LOS}_{\parallel} \mathbf{B}_0$ than that of the $\text{LOS}_{\perp} \mathbf{B}_0$ as the density structures are non-isotropic and are typically shorter along the direction of \mathbf{B}_0 (see §4.1 and Fig. 1). The corresponding L_{dec} is thus smaller for $\text{LOS}_{\parallel} \mathbf{B}_0$, with $L_{\text{dec}} = 4.9 \times 10^{-2}$ and 8.3×10^{-2} for $\text{LOS}_{\parallel} \mathbf{B}_0$ and $\text{LOS}_{\perp} \mathbf{B}_0$, respectively. As we show in §4.3, this difference remains also after time averaging and is seen in all simulations, from small to large k_{drive} and for both considered Mach numbers.

4.3. The decorrelation-scale driving-scale relation

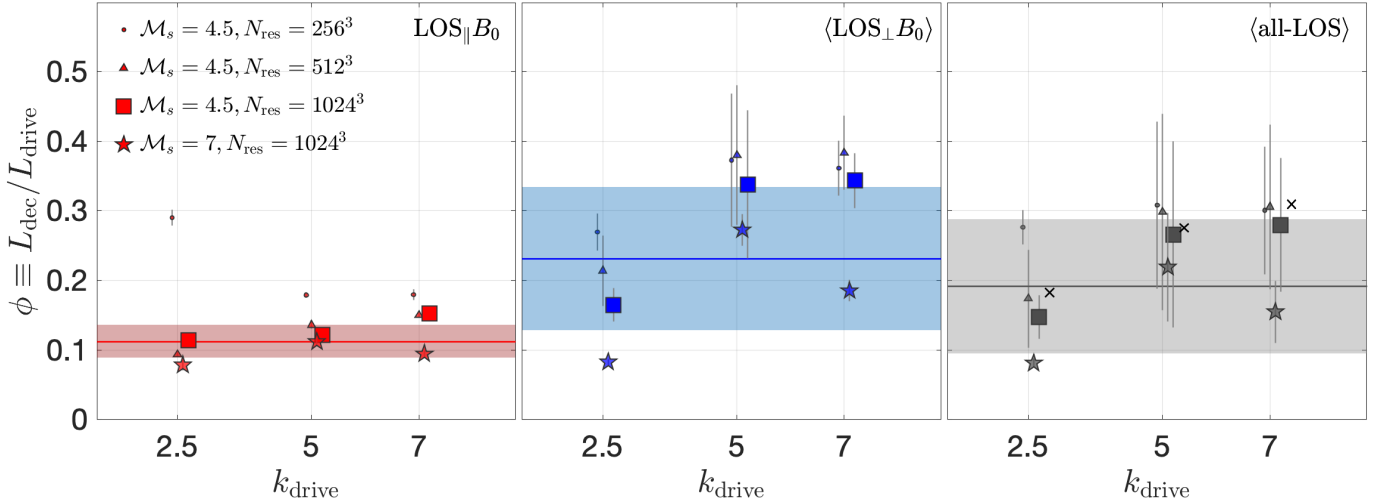


FIG. 3.— The decorrelation-scale to driving-scale ratio, $\phi \equiv L_{\text{dec}}/L_{\text{drive}}$ as a function of driving wavenumber, $k_{\text{drive}} \equiv 1/L_{\text{drive}}$ (in box-length units), as calculated for our set of MHD simulations using the smoothed density method. The three panels correspond to the $\text{LOS}_{\parallel} \mathbf{B}_0$ (left), an average over the $\text{LOS}_{\perp} \mathbf{B}_0$ (middle), and all-LOS average (right). The error bars combine fitting uncertainty and the dispersion over simulation time snapshots and the LOS averaging. The cross symbols in the right panel show the ϕ computed using the auto-correlation function method, for the $\mathcal{M}_s = 4.5$ simulations. In each panel, the horizontal line is the mean ϕ over k_{drive} and \mathcal{M}_s , and the shaded strip is the $\pm 1\sigma$ uncertainty range.

In Fig. 3 we show the ratio $\phi \equiv L_{\text{dec}}/L_{\text{drive}}$ as a function k_{drive} for various resolutions and sonic Mach numbers (different symbols), and LOS orientation: the $\text{LOS}_{\parallel} \mathbf{B}_0$ (left panel), the average over the two $\text{LOS}_{\perp} \mathbf{B}_0$ (middle) and an average over all three LOSs (right). As discussed in §3.2 each L_{dec} is also an average over 5 time snapshots and the error bars are $\pm 1\sigma$ uncertainty ranges, corresponding to quadrature sums of the fitting process error and the SD over the time snapshots. For the left and right panels, the errors are larger as they also include the dispersion over the averaged LOS.

If correlations in the density field are imposed by the driving scale, we expect $\phi \equiv L_{\text{dec}}/L_{\text{drive}}$ to be constant in respect to k_{drive} . Starting from the left panel of Fig. 3 we see that in the case of the $\text{LOS}_{\parallel} \mathbf{B}_0$, ϕ indeed remains nearly constant across k_{drive} and \mathcal{M}_s . The average ϕ over k_{drive} and \mathcal{M}_s (at $N_{\text{res}} = 1024^3$) is

$$\langle \phi \rangle_{\parallel \mathbf{B}_0} = 0.112 \pm 0.024. \quad (5)$$

The error is the $\pm 1\sigma$ uncertainty range, encompassing the dispersion (the SD) across the driving scale, Mach number, simulation time snapshot, summed in quadrature with the fitting procedure error. The mean and the $\pm 1\sigma$ uncertainty range are shown as the red horizontal line and shaded strip in Fig. 3.

For the $\text{LOS}_{\perp} \mathbf{B}_0$ (middle panel) the ϕ values are higher, with

$$\langle \phi \rangle_{\perp \mathbf{B}_0} = 0.23 \pm 0.11, \quad (6)$$

and have a larger uncertainty range. The larger $L_{\text{dec}, \perp \mathbf{B}_0}$, compared to $L_{\text{dec}, \parallel \mathbf{B}_0}$, may be seen by-eye in the density slices presented in Fig. 1, and may be explained by the fact that gas compression is limited in the direction perpendicular to the magnetic field (see §4.1). The SD deviation is also much larger in the $\perp \mathbf{B}_0$ case. Furthermore, ϕ shows an increasing trend with increasing k_{drive} . However, numerical convergence is not optimal for these LOS (as evident by comparing the various resolution markers), and the number of points across k_{drive} is limited. A ϕ that increases with k_{drive} may be expected if the large scale B_0 field induces correlations on large scales proportional to the simulation box length rather than the driving scale.

Finally, in the right panel we show the average L_{dec} over all LOS (with appropriate weights: 2/3 for the $\text{LOS}_{\perp} \mathbf{B}_0$ and 1/3 for the $\text{LOS}_{\parallel} \mathbf{B}_0$). We obtain

$$\langle \phi \rangle_{\text{all LOS}} = 0.19 \pm 0.10, \quad (7)$$

We also calculated the decorrelation lengths from the ACF, by finding the point at which the ACF falls to a fraction $\varepsilon = 0.1$ of its maximal value. This measure was suggested by VG in their study of column density PDFs (which are tightly related to the $x\ell$ distribution). In Fig. 3 we compare ϕ as computed using our smoothed-density method and via the the ACF, for the $\mathcal{M}_s = 4.5$ simulations. Interestingly, the decorrelation length obtained from the ACF agrees well with that obtained with our smoothed-density method. However, while the ACF method depends on the arbitrary choice of ε , our method does not require any tuning as it relies on an analytic model that describes the dependence of $\sigma_{x\ell}(\ell)/\sigma_x$ on L_{dec} (see §2).

5. DISCUSSION

In this Letter we have explored the density structures that arise in a supersonic magnetized driven turbulence box simulations. In particular, we focused on quantifying the relation between the decorrelation scale (L_{dec}) and the turbulence driving scale (L_{drive}) as well as on the orientation relative to the large scale magnetic field. We find that the $L_{\text{dec}} - L_{\text{drive}}$ relation may be approximated by a constant ratio, of $\phi \equiv L_{\text{dec}}/L_{\text{drive}} = 0.19$, on average. If only the LOS parallel to \mathbf{B}_0 is considered, the decorrelation scale is smaller, with $\phi = 0.11$, and the relation is tighter.

5.1. Implications to Observations

In a broader context, the $L_{\text{dec}} - L_{\text{drive}}$ relation is a key component in the quest to constrain turbulence properties from observations. This is depicted in Fig. 4. The diagram shows that the turbulence, the density structure, and the chemical structure of interstellar gas are connected:

- (A) Turbulence (when supersonic) produces strong density fluctuations in the gas such that the properties of the density field depend on the turbulence properties

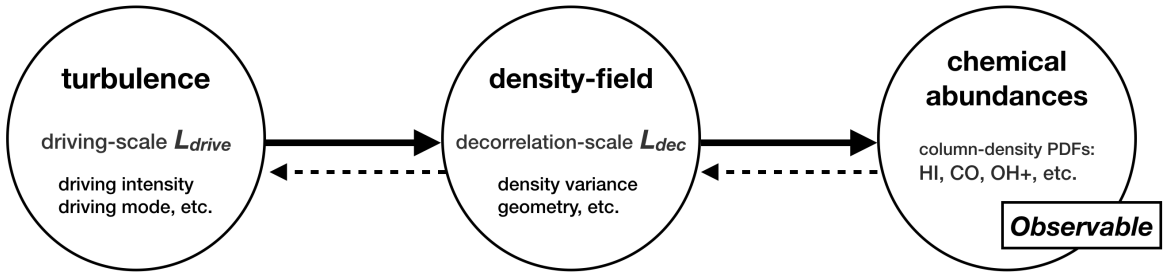


FIG. 4.— Schematic diagram demonstrating how turbulence determines the density field which in turn affects the PDF of chemical abundances (solid arrows). Thus observations of column density PDFs may be used to constrain the density field and turbulence properties (dashed arrows). Therefore it is important to quantify the connections between properties of turbulence driving, the density field, and chemical structure.

- (B) The density structure, in turn, controls the abundances of various chemical species since the rates of chemical reactions are sensitive to gas density.

Thus, we may potentially use observations of chemical abundances to constrain the density field and turbulence properties. For this we need to quantify the (A) and (B) connections in Figure 4 (i.e., the solid arrows). In previous work we investigated connection (B), focusing on how L_{dec} and the sonic Mach number control the abundances of HI (BBS), and the molecular ions OH^+ , H_2O^+ , and ArH^+ (Bialy et al. 2019). In this paper we focused on connection (A) in Figure 4, and established the link between the decorrelation-scale, L_{dec} , and the driving-scale, L_{drive} , via a set of MHD simulations driven on varying scales. More generally, turbulence driving is also described by other parameters, such as the velocity dispersion at the driving scale, and the ratio of solenoidal versus compressional modes, which also affect the density field.

5.2. Limitations and Future Work

In this study we have analyzed 3D MHD driven box simulations with an isothermal equation of state (see §3.1). In the realistic ISM, the density field is affected by active cooling and heating processes, which render the equation of state non-isothermal, and leading to the formation of a multiphase medium composed of cold-dense and warm-diffuse gas (Field et al. 1969; Wolfire et al. 2003; Bialy & Sternberg 2019), although the phase separation vanishes when turbulence is sufficiently strong (Gazol & Kim 2013; Kritsuk et al. 2017). In a future study, it would be interesting to investigate the structure of the density field (i.e., the $L_{\text{dec}} - L_{\text{drive}}$ relation)

in a non-isothermal medium. Other important generalizations is a self-gravitating medium, and the inclusion of feedback (i.e., supernova feedback), which can drive turbulence and provide gas heating. In this study we deliberately used the setup of isothermal, non-gravitational, Fourier-driven simulations, as they constitute a clean numerical experiment that are useful for deriving and understanding the basic form of the $L_{\text{dec}} - L_{\text{drive}}$ relation.

6. CONCLUSION

We found that the decorrelation-scale of the density field, L_{dec} , is related to the turbulence driving scale, following an approximately constant ratio, $L_{\text{dec}}/L_{\text{drive}} \approx \phi$ where $\phi = 0.112 \pm 0.024$ for density fluctuations along the large scale \mathbf{B}_0 field, and with $\phi = 0.23 \pm 0.11$ for fluctuations perpendicular to \mathbf{B}_0 . On average over all directions, $\phi = 0.19 \pm 0.10$. The decorrelation scale calculated with our smoothed density method is in good agreement with that obtained from the autocorrelation function. The $L_{\text{dec}} - L_{\text{drive}}$ relation is a key step for constraining the turbulence driving scale from observations of column density PDFs. This may shed light on the relative importance of various turbulence stirring mechanisms in the Galaxy.

We are grateful for valuable discussions with Amiel Sternberg. We thank the referee for useful suggestions that improved this paper. B.B. acknowledges the generous support of the Simons Foundation Flatiron Institute Center for Computational Astrophysics (CCA). S.B. acknowledges support from the Harvard-Smithsonian Institute for Theory and Computation (ITC) and visitor support from the CCA.

REFERENCES

- Armstrong, J. W., Rickett, B. J., & Spangler, S. R. 1995, *ApJ*, 443, 209
 Balbus, S. A. & Hawley, J. F. 1991, *ApJ*, 376, 214
 Barlow, R. 1989, *A Guide to the Use of Statistical Methods in Physical Sciences* (New York: Wiley)
 Bialy, S., Burkhart, B., & Sternberg, A. 2017, *ApJ*, 843, 92
 Bialy, S., Neufeld, D., Wolfire, M., Sternberg, A., & Burkhart, B. 2019, *ApJ*, 885, 109
 Bialy, S. & Sternberg, A. 2019, *The Astrophysical Journal*, 881, 160
 Burkhart, B., Collins, D. C., & Lazarian, A. 2015a, *ApJ*, 808, 48
 Burkhart, B., Falceta-Gonçalves, D., Kowal, G., & Lazarian, A. 2009, *ApJ*, 693, 250
 Burkhart, B., Lazarian, A., Balsara, D., Meyer, C., & Cho, J. 2015b, *ApJ*, 805, 118
 Burkhart, B., Lee, M.-Y., Murray, C. E., & Stanimirović, S. 2015c, *ApJL*, 811, L28
 Burkhart, B., Stanimirović, S., Lazarian, A., & Kowal, G. 2010, *ApJ*, 708, 1204
 Chepurnov, A., Burkhart, B., Lazarian, A., & Stanimirović, S. 2015, *ApJ*, 810, 33
 Chepurnov, A., Lazarian, A., Stanimirović, S., Heiles, C., & Peek, J. E. G. 2010, *ApJ*, 714, 1398
 Cho, J. & Lazarian, A. 2003, *MNRAS*, 345, 325
 Correia, C., Lazarian, A., Burkhart, B., Pogossyan, D., & De Medeiros, J. R. 2016, *ApJ*, 818, 118
 Elmegreen, B. G. & Scalo, J. 2004, *ARAA*, 42, 211
 Federrath, C., Klessen, R. S., & Schmidt, W. 2008, *ApJ*, 688, L79
 Field, G. B., Goldsmith, D. W., & Habing, H. J. 1969, *ApJL*, 155, L149
 Fischera, J. & Dopita, M. A. 2004, *ApJ*, 611, 919
 Gazol, A. & Kim, J. 2013, *ApJ*, 765, 8
 Goldreich, P. & Sridhar, S. 1995, *ApJ*, 438, 763
 Herron, C. A., Federrath, C., Gaensler, B. M., Lewis, G. F., McClure-Griffiths, N. M., & Burkhart, B. 2017, *MNRAS*, 466, 2272
 Hughes, A., Wong, T., Ott, J., Muller, E., Pineda, J. L., Mizuno, Y., Bernard, J.-P., Paradis, D., Maddison, S., Reach, W. T., Staveley-Smith, L., Kawamura, A., Meixner, M., Kim, S., Onishi, T., Mizuno, N., & Fukui, Y. 2010, *MNRAS*, 406, 2065
 Kowal, G., Lazarian, A., & Beresnyak, A. 2007, *ApJ*, 658, 423
 Kritsuk, A. G., Ustyugov, S. D., & Norman, M. L. 2017, *New Journal of Physics*, 19, 065003
 Krumholz, M. R. 2014, *Phys. Rep.*, 539, 49
 Krumholz, M. R. & Burkhart, B. 2016, *MNRAS*, 458, 1671
 Krumholz, M. R., McKee, C. F., & Tumlinson, J. 2009, *ApJ*, 693, 216

- Lazarian, A. 2007, *Journal of Quantitative Spectroscopy and Radiative Transfer*, 106, 225
- Lazarian, A. & Yan, H. 2014, *ApJ*, 784, 38
- McKee, C. F. & Ostriker, E. C. 2007, *ARAA*, 45, 565
- Offner, S. S. R., Clark, P. C., Hennebelle, P., Bastian, N., Bate, M. R., Hopkins, P. F., Moraux, E., & Whitworth, A. P. 2014, *Protostars and Planets VI*, 53
- Ostriker, E. C., McKee, C. F., & Leroy, A. K. 2010, *ApJ*, 721, 975
- Pingel, N. M., Lee, M.-Y., Burkhardt, B., & Stanimirović, S. 2018, *ApJ*, 856, 136
- Portillo, S. K. N., Slepian, Z., Burkhardt, B., Kahraman, S., & Finkbeiner, D. P. 2018, *ApJ*, 862, 119
- Ross, J., Latter, H., & Tehranchi, M. 2017, *MNRAS*, 468, 2401
- Schlickeiser, R. 2002, *Cosmic Ray Astrophysics*, ed. R. Schlickeiser
- Squire, J. & Hopkins, P. F. 2017, *MNRAS*, 471, 3753
- Vazquez-Semadeni, E. & Garcia, N. 2001, *ApJ*, 557, 727
- Wolfire, M. G., McKee, C. F., Hollenbach, D., & Tielens, A. G. G. M. 2003, *ApJ*, 587, 278
- Xu, S., Yan, H., & Lazarian, A. 2016, *ApJ*, 826, 166